

Unsteady simulation of intake ground vortex ingestion in real wind tunnel conditions

Rita MENDONCA E COSTA ⁽¹⁾, Grégory MILLOT ⁽¹⁾, Sylvain RAYNAL ⁽¹⁾, Jean-Paul BOUCHET ⁽²⁾, Sébastien COURTINE ⁽²⁾

⁽¹⁾ ALTRAN, 4 Avenue Didier Daurat 31700 BLAGNAC, FRANCE, Email:

rita.jesusedmendoncaecosta@altran.com, gregory.millot@altran.com, sylvain.raynal@altran.com

⁽²⁾ CSTB, 11 rue Henri Picherit – BP82341 44323 NANTES Cedex 3 FRANCE, Email:

JeanPaul.BOUCHET@cstb.fr, Sebastien.COURTINE@cstb.fr

ABSTRACT

The present article focuses on the analysis of vortex ingestion phenomenon by a nacelle placed in a real WT geometry (Jules Verne Wind Tunnel, CSTB). Flow details are investigated for a specific set of parameters (intake speed, wind speed, and ground clearance) and compared to an isolated nacelle with the same set of parameters. The developed methodology for vortex post-processing (namely, monitoring of relevant parameters) is also presented, and applied to the calculations with the nacelle in the WT configuration. Main results outline the similarities of the flow in both studied configurations (isolated/ WT), and the milestones achieved in vortex monitoring with the developed post-processing methodology.

1. INTRODUCTION

The present study focuses on the analysis of vortex formation and ingestion by aircraft engines in ground operations. This phenomenon arises under specific combinations of wind direction and velocity, and inlet air speed, generating engine vibrations and leading to suction of abrasive particles; thus, its characterization in early design stages is crucial. This behaviour has been reviewed in the literature in the work of [1], [2], [3], [4], [5], [6], [7].

The framework of this investigation is the InVIGO project (EU CleanSky2 Programme). This project combines wind tunnel (WT) test results with RANS (Reynolds-Averaged Navier-Stokes) and Hybrid (SAS – Scale Adaptive Simulations) numerical simulations performed in a full wind-tunnel geometry, to provide a comprehensive characterization of vortex ingestion. The final goal is to develop a predictive model for vortex formation using data analytics and apply it during engine tests with conventional “light instrumentation” (pressure

rakes, generally used to capture large flow separation regions).

2. WIND TUNNEL CONFIGURATION

The Jules Verne Climatic Wind Tunnel (WT), operated by CSTB in Nantes (France), is made of two circuits as illustrated on Fig. 1:

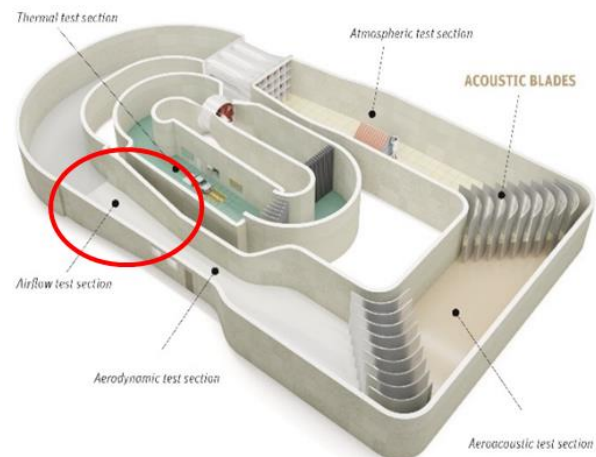


Figure 1. Jules Verne Climatic Wind Tunnel.

The external ring called “dynamic circuit” and, in particular the “aerodynamic” test section (30m², maximum wind speed of 75m/s, turbulence intensity <2%) is perfectly suitable to reproduce the expected wind conditions on a representative nacelle mock-up. In order to reproduce the flow rate in the nacelle (up to 17kg/s), a high-performance fan (250kW) had to be implemented in the wind tunnel. The dimensions of the WT allow this fan to be positioned far downstream in the test section so that neither the presence of the fan nor the exhaust flow disturb the upstream flow perceived by the nacelle. These verifications were achieved by several

numerical simulations which are not presented in this paper. The entire test section thus comprises a long duct, (20 m long), connecting the fan to the air inlet via a 90° elbow to orient the nacelle in a crosswind configuration. A movable, raised floor and a set of optical supports complete this experimental apparatus illustrated in Fig. 2 and Fig. 3:

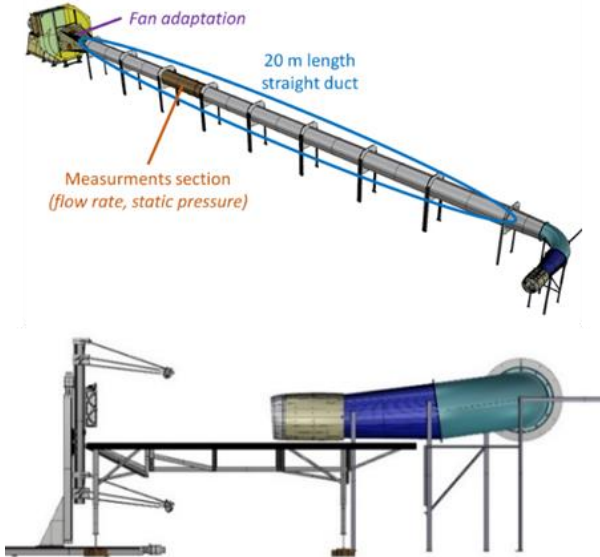


Figure 2. Nacelle mock-up and piping system used in the InVIGO WT experiments.

The first test campaign of the InVIGO project was carried out in December 2020 and made it possible to study the vortex phenomenon in various configurations using total and static pressure instrumentation (130 channels), visualization techniques and Stereo PIV.



Figure 3. WT setup implementation.

3. COMPUTATIONAL DOMAINS AND GENERATED GRIDS

The first setup that was considered in the early stages of the study featured an isolated scaled nacelle, with a diameter of 37 cm (measured at the reference fan plane, $D_{nacelle} = 37cm$). The nacelle was placed at the centre of a sufficiently large cylindrical domain ($D_{cylinder} = 50 D_{nacelle}$). The main purpose of studying the isolated configuration was to provide a baseline for further

comparison with the complete wind tunnel configuration. The generated grid for this baseline case (Fig. 5) comprised a total of 47M elements. The boundary layer in the nacelle walls and on the ground of the domain was resolved using 20 layers of prism elements, with a transition ratio of 0.272 and a growth rate of 1.35. This guaranteed a value of $y^+ < 3$, which allowed resolving all the viscosity affected region down to the wall (using the selected turbulence model).

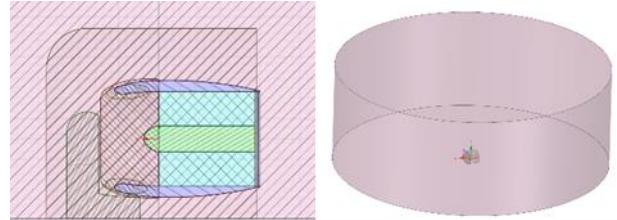


Figure 4. Bodies of Influence (BOI) used for local grid refinement in the vicinity of the nacelle/ground (left) and computational domain used for the isolated configuration (right).

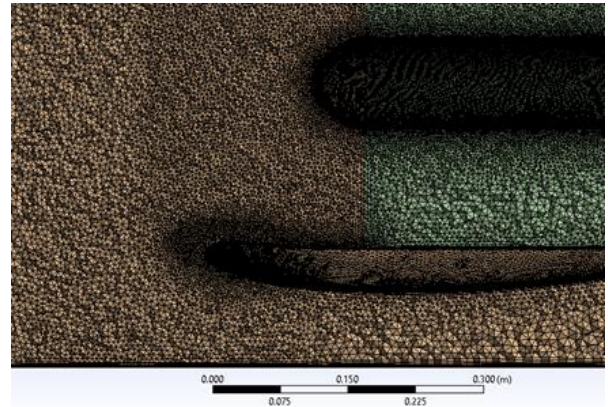


Figure 5. Grid detail in the vicinity of the nacelle for the isolated configuration.

The WT configuration (Fig. 6) featured the real geometry of the Jules Verne Wind Tunnel, which has a constant cross-section part (dimensions 6 m × 5 m × 12 m), followed by a diverging section.

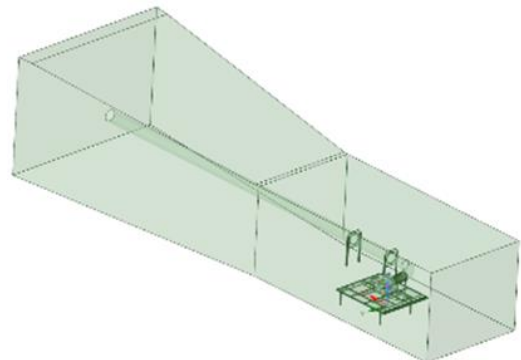


Figure 6. Computational domain for the wind tunnel configuration.

Furthermore, a raised floor under the nacelle (to allow the testing of different ground clearance values) was also included, as well as the piping system connecting the

nacelle outlet to the WT outlet. This system comprised several elements: a first diverging section, an elbow, a second diverging section, and a long, constant diameter section (Fig. 6). The generated grid for this configuration had a total of 57M elements (Fig. 7). The boundary layer on the nacelle walls, on the raised floor, and exterior surface of the two diverging sections + elbow was resolved using the same parameters previously described for the isolated configuration.



Figure 7. Grid detail in the vicinity of the nacelle for the WT configuration.

4. PROBLEM FORMULATION AND NUMERICAL SETUP

4.1. Problem formulation

As for the solution procedure, a steady (RANS) formulation was adopted, using the $k\omega$ -SST turbulence model for closure. It shall be outlined that both configurations (isolated and wind tunnel) were first simulated using a steady-state approach in order to provide a reference solution from which an unsteady calculation could then be performed. Moreover, it was considered (in the general framework of the InVIGO project) that it would be relevant to compare the quality of an averaged, steady-state solution, with the result yielded by an unsteady calculation.

The SAS (Scale Adaptive Simulations) formulation was chosen for the unsteady calculations, due to its inherent benefits in this type of physical problems. Many authors have previously investigated the benefits of using an unsteady approach to treat vortex phenomena, namely: [8], [9], [10]. Before performing the calculations, it was considered relevant to verify if the generated grids were sufficiently fine to allow for proper resolution of turbulence scales. To this end, the Kolmogorov (length) scale was compared to the cell size in vortex vicinity, and the characteristic time scales of the problem were also investigated. This analysis allowed determining that the observed vortex length scales were slightly larger than the grid size at corresponding locations; also, the range of time scales of interest was also determined, providing a basis for the choice of an appropriate timestep (1×10^{-4} s) in the unsteady calculations. This step of verification is herein omitted for the sake of brevity.

4.2. Numerical setup

In the steady simulations, the pressure-velocity coupling was handled using a coupled scheme; as for spatial discretization, second order upwind schemes were used for the pressure and momentum equations, as well as for density and turbulence variables of interest (turbulence kinetic energy and specific dissipation rate).

For the unsteady calculations, using a SAS formulation, a coupled scheme was also used to handle pressure-velocity coupling; as for spatial discretization, a second order scheme was used to discretize the pressure equation, and a bounded central differencing scheme was used for the momentum equation. A second order upwind scheme was used for density, turbulence kinetic energy and specific dissipation rate.

As for the applied boundary conditions (BC), the wind velocity (10 m/s at a 90° angle for crosswind conditions) was imposed at the inlet of the computational domain (for the WT configuration) and at the lateral surface of the cylindrical domain (for the isolated nacelle configuration). A pressure-outlet condition was imposed at the outlet of the nacelle (for both configurations). It shall be mentioned that for the WT configuration, the flow inside the piping system was also simulated (thus imposing the pressure-outlet condition at the outlet of the piping system), and the results compared to the ones obtained with a pressure-outlet condition applied directly at the nacelle outlet. It was observed that the piping did not cause significant flow distortion on the planes of interest for vortex analysis; hence justifying the adoption of the latter modelling choice.

During the first part of the calculation, a pressure-outlet condition with target mass-flow rate was prescribed to the nacelle outlet, followed by the assignment of an appropriate pressure value, up to the end of the simulation.

At the outlet of the WT (end of the WT diverging section), and at the top surface of the cylindrical domain of the isolated configuration domain, a pressure-outlet BC – corresponding to ambient, non-disturbed conditions – was prescribed. The selected test point for analysis in this document had a ground clearance ratio $H/D_{nacelle}$ (ratio between engine axis distance to the ground and $D_{nacelle}$) of 0.85, and an intake speed to wind speed ratio (U^*) of 8.5.

5. RESULTS

5.1. Comparison between isolated and WT configurations

As previously mentioned, the unsteady calculations were performed using the SAS for both analysed configurations, WT (Wind Tunnel) and isolated. Both configurations had identical ground clearance and wind speed (in both magnitude and angle of incidence).

The influence of the number of iterations at each timestep was investigated at an early stage of the study, so that an appropriate value could be selected. Two different options were considered - the use of 2 or 5 iterations per

timestep – and it was found that while the latter did not significantly improve accuracy on the monitored values (namely, pressure and mass flow rate at the nacelle intake), it significantly increased the required CPU time. Hence, the former value (2) was selected.

For both configurations, a calculation up to 0.79s of physical flow time was performed, in order to compare monitored variables. Fig. 8 displays the evolution of the instantaneous and backwards average mass flow rate values, as well as the percentual difference in the average values for both configurations (measured on the right hand-side vertical axis). For each instant, the backwards average represents the average of values comprised between that instant and the final instant. This analysis allowed a confirmation that the functioning point was approximately identical for both configurations: since ground clearance and wind speed were kept constant for both setups, an intake mass flow rate within a difference of 1 % between the two cases ensured the viability of the comparison.

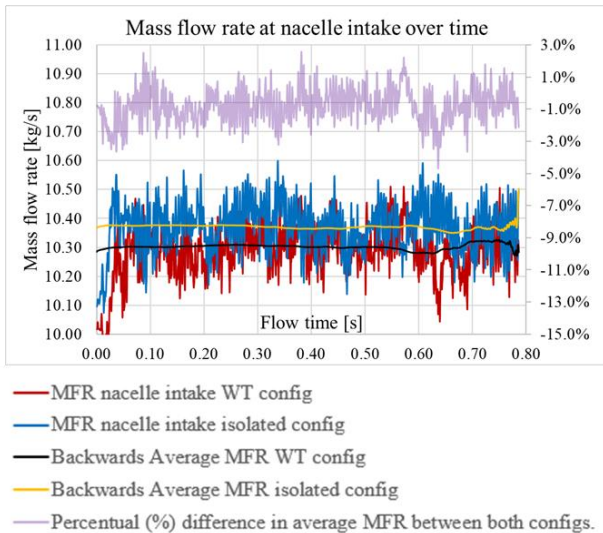


Figure 8. Evolution of the mass flow rate (MFR) as a function of flow time for the unsteady simulations: WT and isolated configurations.

Fig. 9 and Fig. 10 display the path lines incoming from the ground underneath the nacelle (Fig. 9) and entering the nacelle reference fan plane (Fig. 10). Fig. 9 clearly displays the path lines in agreement with the formation and ingestion of a vortical structure (originating from the ground) and Fig. 10 shows the separation region visible on the fan plane, on the side facing the wind.

Fig. 11 and Fig. 12 display the path lines for the isolated configuration, showing the same phenomena previously identified for the WT configuration.

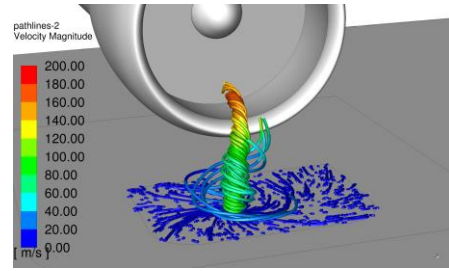


Figure 9. Path lines (coloured by velocity magnitude) originating from the raised floor in the vicinity of the nacelle (BOI), for the WT configuration. Solution at flow time of 0.79s.

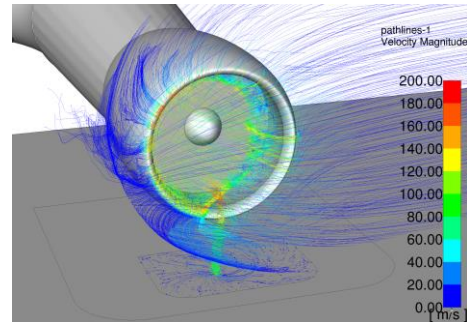


Figure 10: Path lines (coloured by velocity magnitude) entering the reference fan plane, for the WT configuration. Solution at flow time of 0.79s.

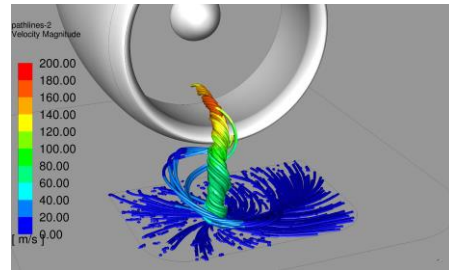


Figure 11. Path lines (coloured by velocity magnitude) originating from the ground in the vicinity of the nacelle (BOI), for the isolated configuration. Solution at flow time of 0.79s.

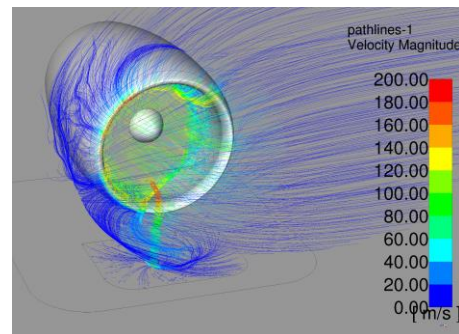


Figure 12. Path lines (coloured by velocity magnitude) entering the reference fan plane, for the isolated configuration. Solution at flow time of 0.79s.

Finally, Fig. 13 shows the total pressure distributions on the reference fan plane, for both configurations, at a physical flow time of 0.79s. These visualizations confirm that the extension of the separated region is identical in both setups, and that the vortex location on this reference plane is also approximately the same. Nevertheless, a slight difference in the total pressure values at the vortex core appears to exist, hinting at a potentially stronger vortex on the WT configuration. However, it shall also be taken into account that the intrinsically unsteady nature of this type of coherent structure causes the vortex to oscillate in terms of position and intensity throughout the simulation, which disrupts the comparison between the two different setups at identical physical flow times.

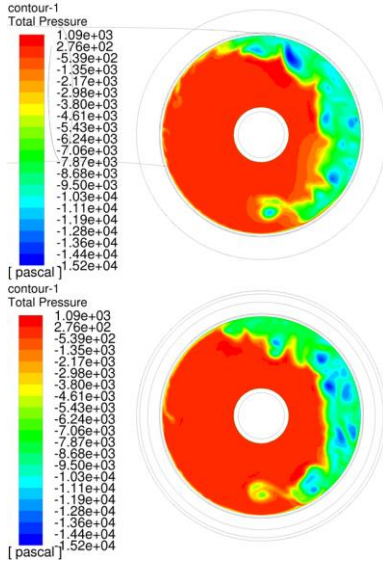


Figure 13. Total pressure distribution (relative to undisturbed pressure) on the reference fan plane for the WT (top) and isolated (bottom) configuration. Solution at flow time of 0.79s.

5.2. Post-processing strategies: distortion indexes to locate vortex centre

One of the main goals of the InVIGO project focused on accurately capturing and monitoring vortex properties along the course of a CFD simulation. Amongst the most relevant quantities to be monitored featured vortex position, radius, and intensity.

Determining the position of the centre of the vortex on a given reference plane (usually, a plane called “fan plane” located at a hypothetical position inside the nacelle, just after the inlet lips) is a task that has been carried out by several authors, namely [1], [3], [11], [12], and relies deeply on a definition of distortion indexes on this reference fan plane. Usually, two different indexes are of interest, to express radial and azimuthal distortion: the IDC, and the DC_θ , respectively. They are classically defined as follows:

$$DC_\theta = \frac{P_f - P_\theta}{q_f} \quad (1)$$

$$IDC = \max_{r \in [0, r_{max}]} \frac{\overline{P_{t,r}} - P_{t,r,min}}{\overline{P_t}} \quad (2)$$

The IDC is defined as the maximum difference between the total pressure averaged along the points of a ring of radius r ($\overline{P_{t,r}}$), on the reference fan plane, and the minimum total pressure on the same set of points ($P_{t,r,min}$), non-dimensionalized by the average total pressure ($\overline{P_t}$) on the entire reference fan plane.

As for the azimuthal distortion index DC_θ , it is defined as the difference between the average total pressure at the fan plane (P_f) and the minimum average total pressure in a sector corresponding to a certain angle θ (P_θ), non-dimensionalized by the average dynamic pressure on the fan plane, q_f .

To benefit from the use of these indexes to determine vortex location, an automated strategy that determined local maxima of both indexes on the fan plane was devised and used for the steady calculations. Through the analysis of different test cases, it was found that computing both indexes using the static pressure (instead of the total pressure, as classically defined) allowed a clear and unequivocal determination of the vortex centre (namely, in cases where a significant separation region was present in immediate adjacency to the nacelle intake lip).

5.3. Vortex monitoring: Q-criterion iso-clips

As it was previously mentioned in section 5.2, one of the main goals of the InVIGO project focused on live tracking of vortex properties throughout the CFD simulations.

Due to its unsteady nature, finding the appropriate combination of criteria to accurately locate vortex position/size and, moreover, tracking these quantities over the course of time are difficult tasks.

The first step that was carried out during the post-processing of the performed calculations was devising an appropriate strategy to locate the coordinates of the vortex centre. As mentioned previously in section 5.2, the use of the absolute maxima of the distortion indexes IDC and DC_θ – computed with the static pressure instead of the total pressure – allowed a correct identification of vortex radial and azimuthal coordinates in most of the tested cases. Nevertheless, it was found that in most of the unsteady simulations, this criterion still identified spurious local pressure minima on the separation region of the fan plane, without correctly capturing vortex location. Hence, a second verification (on a limited angular sector centred at the vortex location determined for the steady solution) using the detection of Q-criterion local maxima ensured that only the vortex centre was captured, successfully removing the influence of the large separation region commonly present in most cases. The Q-criterion is defined as:

$$Q = \frac{1}{2}(\|\Omega^2\| - \|S^2\|) \quad (3)$$

with Ω being the vorticity tensor and S being the strain rate tensor [13]. A vortex core is defined as a region for which $Q > 0$ is observed.

It shall be outlined that, due to the large amounts of data generated by the project – several test cases, at different combinations of intake speeds, wind speeds, and ground clearance values – the automation of vortex detection strategies proved to be of key importance, in order to efficiently post-process all calculations and drastically reduce the time required to analyse the simulations.

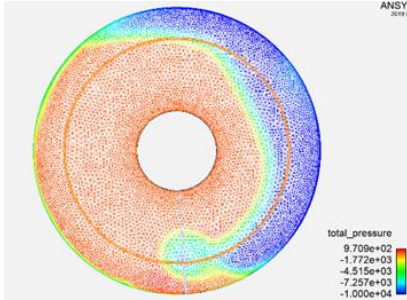


Figure 14. Example of vortex centre detection at the end of the steady simulation: radial and azimuthal position determined automatically.

Since all the performed simulations featured a first steady part – all calculations were run for 6000 to 10000 iterations using a steady, RANS formulation, to obtain a more converged solution before performing the calculations using SAS – the end of the steady simulation provided a first determination of vortex centre location. Fig. 15 shows Q-criterion distribution snapshots on the fan plane, taken at regular intervals throughout the unsteady simulation. While the originally determined vortex location (determined at the end of the steady simulation) does not appear to change dramatically over the course of time, occasional shifts in position and interference with the separation region on the right hand side of the nacelle lip are visible.

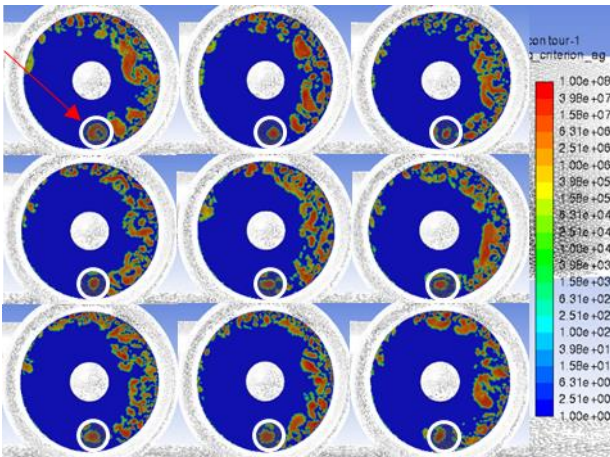


Figure 15. Reference fan plane Q-criterion distributions (log scale) taken at equal intervals up to 0.1965s of flow time. Vortex region highlighted with a white circle.

With this type of behaviour, it proved necessary to devise a tracking strategy that would follow the vortex movement without capturing the resolution of additional structures on the separated region. To this end, several steps were carried out.

The first step consisted in defining a circular region, centred on the pre-determined vortex centre, with a radius large enough to produce a quasi-tangent circle to the extremity of the reference plane: either the plane where Particle Image Velocimetry (PIV) measurements were taken during experimental tests, or the reference fan plane. For the fan plane, a small margin (to avoid absolute tangency) was included, in order to avoid capturing the boundary layer region, in adjacency to the nacelle lip, which usually contains very strong values of Q-criterion – potentially even higher than those found at the vortex core.

Secondly, a set of approximately 10 iso-clips - based on the Q-criterion value – were created in the previously defined circular region, according to the values defined in Tab. 1. The maximum value of the set of minimum thresholds – represented as $2 \times 10^7 \text{ s}^{-1}$ on Tab. 1 - had to be adjusted according to the maximum value of Q-criterion at the vortex core at the end of the steady simulation, on each plane being considered. The Q-criterion maximum threshold – set as $6 \times 10^{12} \text{ s}^{-1}$ – was deemed large enough to capture the vortex core at all times, according to observation on the several test runs that were carried out.

During the simulation, several variables were monitored on each of these 10 iso-clips:

- The area of each of the clips.
- The circulation (computed as the surface integral of the vorticity component perpendicular to each one of the reference planes).
- The area-weighted average coordinates of each one of the clips.

The monitoring of these variables was performed at every 5 timesteps. This value was chosen as a compromise between accuracy and required CPU time. The monitoring strategy was applied on the fan plane and on each one of the PIV reference planes (as displayed in Fig. 16).

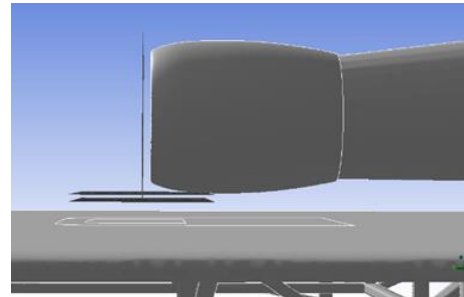


Figure 16. Placement of additional reference planes (corresponding to the experimental location of PIV - particle image velocimetry planes) to provide additional monitoring of vortex properties.

Table 1. Definition of the Q-criterion iso-clips to be performed on the circle.

Q-criterion iso-clip minimum threshold [s ⁻¹]	Q-criterion iso-clip maximum threshold [s ⁻¹]
1 × 10 ³	6 × 10 ¹²
1 × 10 ⁴	6 × 10 ¹²
1 × 10 ⁵	6 × 10 ¹²
2 × 10 ⁵	6 × 10 ¹²
5 × 10 ⁵	6 × 10 ¹²
1 × 10 ⁶	6 × 10 ¹²
2 × 10 ⁶	6 × 10 ¹²
5 × 10 ⁶	6 × 10 ¹²
1 × 10 ⁷	6 × 10 ¹²
2 × 10 ⁷	6 × 10 ¹²

At the end of the simulation, the area and circulation values monitored throughout the calculation were used to compute an equivalent vortex radius:

$$r_{eq} = \sqrt{\frac{A_{clip}}{\pi}} \quad (4)$$

And V_θ , an indirect measure of vortex intensity, given by:

$$V_\theta = \frac{\Gamma}{2\pi r_{eq}} \quad (5)$$

in which Γ is the monitored circulation, calculated for each one of the clips. For each instant of the simulation, a different value of V_θ is obtained for each of the clips (corresponding to a given equivalent radius); the clip corresponding to the maximum value of V_θ yields the equivalent vortex radius (Fig. 17).

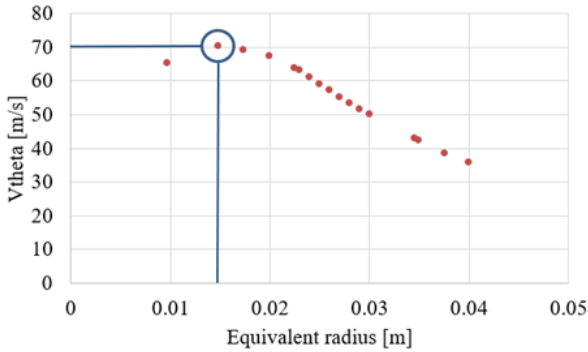


Figure 17. V_θ as a function of Q-criterion clip equivalent radius, for a given instant of the simulation.

It was then possible to analyse the evolution of these two quantities (equivalent vortex radius and V_θ) over the course of time, for both isolated and WT configurations, and for all reference planes: fan plane and vertical/horizontal PIV planes. The results obtained for the fan plane are displayed in Fig. 18; the results obtained for the PIV planes are herein omitted for the sake of brevity.

The variables of interest appear to be in fair agreement for both configurations; however, the multiple oscillations observed for both setups motivated a deeper

analysis of the selected methodology to monitor these quantities. Fig. 19 highlights one difficulty associated with the selected methodology: in fact, the Q-criterion iso-clips with lowest inferior threshold comprise a small part of an additional resolved structure in the vicinity of the vortex, for the particular instant selected, hence affecting the estimation of vortex radius and associated V_θ . Nevertheless, it was observed that the vortex centre coordinates determination was not significantly affected by this aspect. Since the tracking of the vortex centre is obtained through an area-weighted average of the several iso-clips, the coordinates given by the Q-criterion iso-clip with smallest area (that is, the iso-clip corresponding to the highest Q-criterion values), which encircles the vortex core, can be considered relatively accurate and provide useful monitoring information throughout the simulation. The evolution of these quantities during the performed simulations is herein omitted for the sake of brevity.

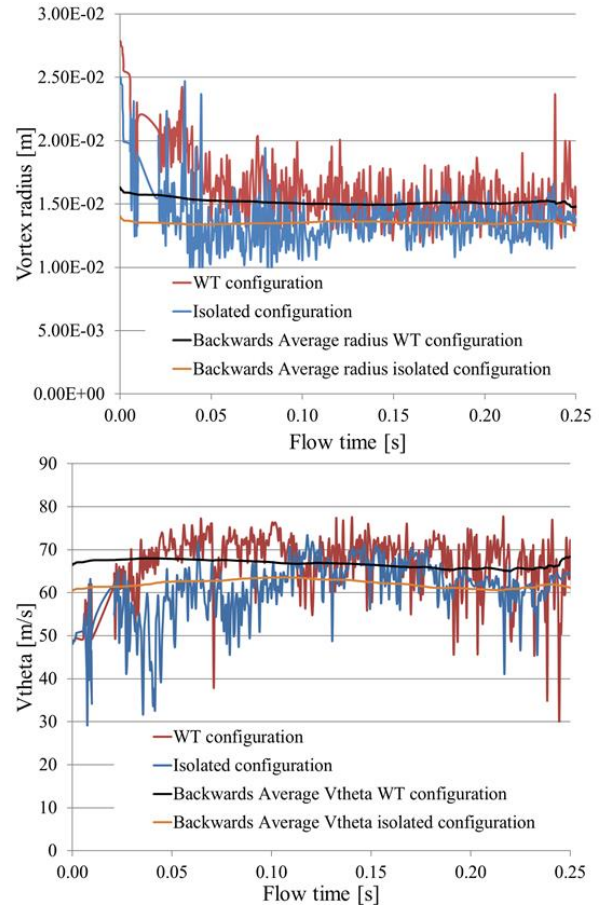


Figure 18. Evolution of vortex radius (top) and V_θ (bottom) over the course of time for both isolated and WT configurations, on the fan reference plane.

5.4. Vortex monitoring: Integration of vorticity on several circular clips

Another strategy that was also investigated to monitor vortex related quantities (namely, vortex radius and V_θ) consisted in adopting a more classical post-processing approach, and hence treating the obtained results at the

end of the simulation, without the “live-monitoring” that was described in the previous subsection.

This approach required saving several solution files throughout the simulation to then perform the following:

- Calculate vortex centre coordinates for each of the instants.
- Integrate the normal component of the vorticity in several circular clips, with increasing radius (centred at the determined coordinates),
- Calculate V_θ for each clip and determine the equivalent vortex radius, based on the procedure described in the previous subsection.

The main advantage of this approach lies on the fact that no real live tracking is required, hence the vortex centre can be determined precisely for each one of the retrieved the solution files. However, this method also requires the storage of large volumes of data (since the post-processing steps concerning the integration of the vorticity are performed directly using *ANSYS Fluent*).

Another shortcoming to be taken into consideration is the fact that vortex shape (since it is hardly ever perfectly circular) is poorly accounted for using the integration on circular clips. Nevertheless, it was considered that using a sufficiently large set of clips (with small increments in the radius value) could potentially avoid the capturing of additionally resolved structures in vortex vicinity, which would represent a significant advantage when compared to the procedure described in the previous subsection.

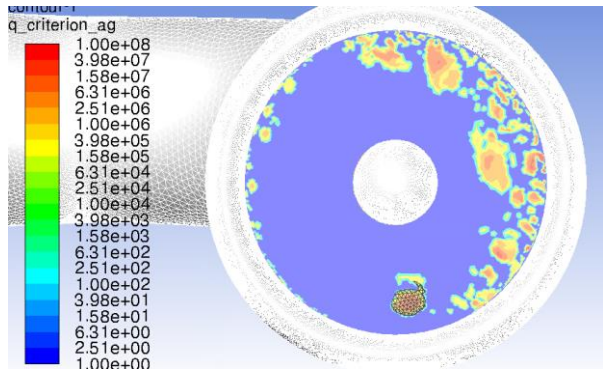


Figure 19. Q-criterion distribution (log scale) on the reference fan plane; representation of lowest threshold Q-criterion iso-clip.

To analyse the viability of this option, the WT configuration was selected (since it was more representative of the real configuration used within the scope of the InVIGO project), and 11 solution files were retrieved up to a flow time of 0.2565s.

The equivalent vortex radius and V_θ were computed for the 11 retrieved instants and compared to the values obtained at the same instants using the Q-criterion iso-clips method. This exercise was performed for two of the reference planes (fan and vertical PIV). The vortex radius values obtained with the circular clips’ method are herein omitted.

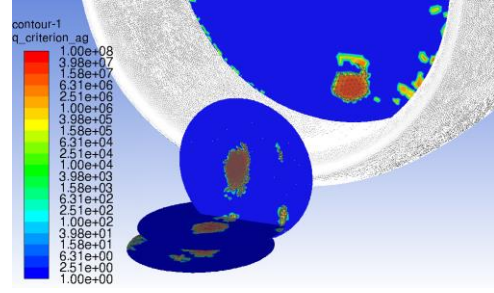


Figure 20. Q-criterion distribution (log scale) on fan plane, vertical and horizontal PIV planes; representation of lowest threshold Q-criterion iso-clip.

However, values found in the literature [3] were taken as a reference for comparison with the results obtained with the Q-criterion clips method. In [3], the vortex radius was found to be comprised between $0.05D_i$ and $0.06D_i$, being D_i the diameter of the reference inlet plane. In the present study, and using the diameter of the reference plane ($D_{nacelle} = 37\text{cm}$), values between 1.85 cm and 2.22 cm should be found, which relatively agrees with the data displayed in Fig. 18. Naturally, the capturing of additional resolved structures in the fan plane affects the estimation of vortex radius for certain instants, which predictably explains the differences between the reference (literature) values and the obtained results.

Table 2. Comparison of V_θ values obtained using the Q-criterion clips method and the circular clips method, for the reference fan plane (SI units).

Flow time [s]	V_θ with Q-criterion clips method [m/s]	V_θ with circular clips method [m/s]	Difference
0.0565	76.14	65.60	14 %
0.0765	75.22	70.45	6 %
0.0965	73.65	62.87	15 %
0.1165	67.01	65.88	2 %
0.1365	67.69	60.21	11 %
0.1565	54.99	65.13	18 %
0.1765	69.79	64.37	8 %
0.1965	72.06	64.53	10 %
0.2165	68.82	65.09	5 %
0.2365	72.19	65.17	10 %
0.2565	74.28	64.46	13 %

Table 3. Comparison of V_θ values obtained using the Q-criterion clips method and the circular clips method, for the reference PIV plane (SI units).

Flow time [s]	V_θ with Q-criterion clips method [m/s]	V_θ with circular clips method [m/s]	Difference
0.0565	81.99	84.94	4 %
0.0765	81.76	78.10	4 %
0.0965	77.33	75.73	2 %
0.1165	77.07	73.62	4 %
0.1365	75.85	72.53	4%
0.1565	73.98	69.76	6 %
0.1765	73.74	70.95	4 %
0.1965	71.96	72.18	0 %
0.2165	73.35	71.88	2 %
0.2365	70.62	73.85	5 %
0.2565	73.10	74.66	2 %

The results shown in Tab. 2 & Tab. 3 show that for V_θ , there appears to be a fair agreement between the results yielded by both methods: Q-criterion and circular clips. Naturally, in the fan plane, the resolution of additional structures (as seen in Fig. 21) makes it difficult to obtain close values for all selected instants; however, in the PIV plane, with a better isolated vortex imprint (Fig. 21), the methods are in quite good agreement.

6. CONCLUSION AND FUTURE WORK

The present work provided a comparison between the unsteady simulation of ground vortex formation and ingestion for two different configurations: one with an isolate nacelle in a selected computational domain, and a second one featuring the nacelle integrated in a real Wind Tunnel configuration (Jules Verne Wind Tunnel, CSTB). Both setups were compared at identical operating points (identical ground clearance, wind speed and angle of incidence, and identical intake mass flow rate).

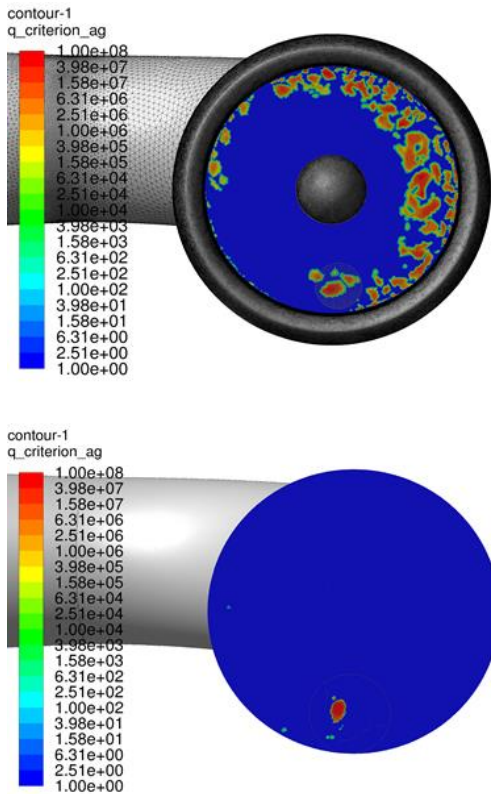


Figure 21. Distribution of Q-criterion values (log scale) on the fan (top) and vertical PIV plane (bottom) for flow time = 0.2365 s.

The comparison between the flow characteristics in both setups showed that no major differences were found between the two, proving that the presence of additional elements in the Wind Tunnel setup (piping connecting the nacelle to the suction system, raised floor/table to simulate different values of ground clearance) and the geometry of the experimental facilities itself did not significantly affect the formation and ingestion of a ground vortex for the selected test points. Moreover, the presence and capturing of a lateral separation region in

immediate adjacency to the nacelle internal lip was also identical for both configurations.

These findings support the evidence that vortex phenomena can safely be studied in a simplified configuration (such as the one of the isolated nacelle) without compromising the accurate representation of the phenomena. This brings a clear advantage in studies in which several configurations (namely, with several ground clearance values) are to be tested, since it allows for the use of locally refined grids, with resolution of the boundary layer up to the walls in the nacelle vicinity only. Concerning the developed post-processing strategies, used to identify vortex location and perform live tracking of relevant associated properties, most significant milestones included:

- Automated determination of vortex centre for any given solution.
- Tracking of vortex centre, radius, and V_θ over the course of a simulation.

It shall be outlined that the devised methodology to monitor vortex radius and V_θ (successive iso-clips of different Q-criterion thresholds, applied on a limited circular region centred on the pre-determined vortex centre) proved to accurately isolate the vortex in steady simulations, where there is no resolution of additional structures on the separated region and hence the risk of interaction with the studied vortex is smaller (Fig. 22).

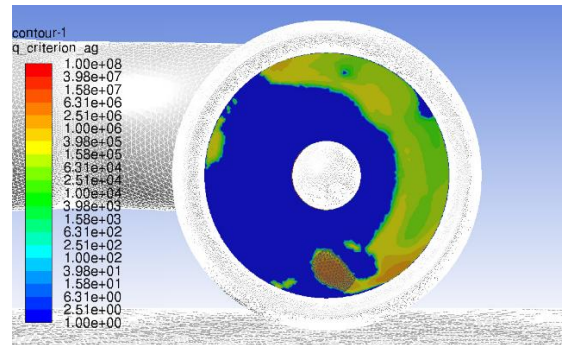


Figure 22. Example of Q-criterion clip accurately capturing the vortex region in a steady simulation.

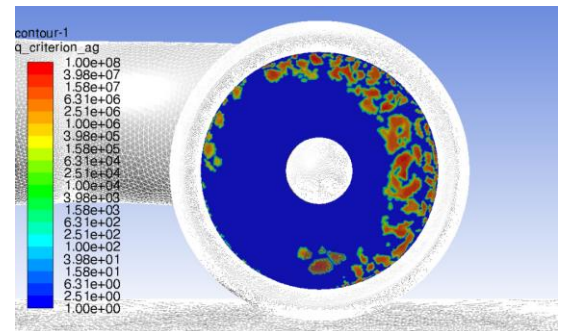


Figure 23. Example of Q-criterion clip capturing multiple resolved structures in the vortex region in an unsteady simulation.

However, in unsteady simulations, this method still captured unwanted additional structures for some of the simulation instants (Fig. 23). Nevertheless, it was considered that the average values of these parameters over the entire simulation time could still be an

acceptable estimation, helping in vortex characterization for each of the test cases.

Future work will include an improvement of the tracking strategy for unsteady simulations, predictably through the detection of Q-criterion iso-contours beginning at the vortex centre and progressively moving outwards, in order to compute circulation in each region enclosed by each Q-criterion contour. This type of post-processing will predictably yield more accurate results, (since it will avoid the capturing of additional resolved structures) however invalidating the possibility to live-track vortex properties without any *a priori* knowledge from each simulation: reference plane (fan, PIV) data will have to be retrieved periodically and analysed *a posteriori* in order to compute vortex relevant quantities (V_θ , radius).

7. ACKNOWLEDGEMENTS

The project leading to this application has received funding from the Clean Sky 2 Joint Undertaking under the European Union's Horizon 2020 research and innovation program under grant agreement No [864288]. This communication and the data provided here represent only the authors' view and do not engage Clean Sky 2 nor the European Union for any use that may be made of the information they contain.



We would also like to thank Safran Aircraft Engines for their involvement on this project.

8. REFERENCES

1. Zantopp, S., MacManus, D., & Murphy, J. (2010). Computational and experimental study of intake ground vortices. *The Aeronautical Journal*, vol. 114, no. 1162, 769-784.
2. Yadlin, Y., & Shmilovich, A. (2006). Simulation of Vortex Flows for Airplanes in Ground Operations. 44th AIAA Aerospace Sciences Meeting and Exhibit. Reno, Nevada.
3. Murphy, J. (2008). Intake Ground Vortex Aerodynamics. Cranfield University.
4. Mishra, N., MacManus, D., & Murphy, J. (2011). Intake ground vortex characteristics. Proceedings of the Institution of Mechanical Engineers, Part G: *Journal of Aerospace Engineering*, vol. 226, no. 11 (pp. 1387-1400). doi:10.1177/0954410011424092.
5. Trapp, L., & Girardi, R. (2012). Evaluation of Engine Inlet Vortices Using CFD. 50th AIAA Aerospace Sciences Meeting. Nashville, Tennessee: American Institute of Aeronautics and Astronautics.
6. Secareanu, A., & Moroianu, D. (2005). Experimental and Numerical Study of Ground Vortex Interaction in an Air-Intake. 43rd AIAA Aerospace Sciences Meeting and Exhibit. Reno, Nevada: American Institute of Aeronautics and Astronautics.
7. Sadoudi, Y. (2016). Simulation numérique de l'interaction soufflante/nacelle en présence de vent de travers. Toulouse, France: Université Fédérale Toulouse Midi-Pyrénées.
8. Wang, Z., & Gursul, I. (2012). Unsteady characteristics of inlet vortices. *Experiments in Fluids*, 1015-1032.
9. Yang, Z. (2014). Assessment of unsteady-RANS approach against steady RANS approach for predicting twin impinging jets in a crossflow. *Cogent Engineering*, 1:1, 936995, doi:10.1080/23311916.2014.936995.
10. Tanguy, G., MacManus, D., Garnier, E., & Martin, P. (2018, July). Characteristics of unsteady total pressure distortion for a complex aero-engine intake duct. *Aerospace Science and Technology*, 78, 297-311.
11. Shin, H., Greitzer, E., & Cheng, W. (1986). Circulation measurements and vortical structure in an inlet-vortex flow field. *Journal of Fluid Mechanics*, 162, 463-487.
12. Zachos, P., MacManus, D., & Chiereghin, N. (2016). Flow Distortion Measurements in Convolved Aero Engine Intakes. *AIAA Journal*, 54(9), 2819-2832. doi:10.2514/1.J054904
13. Joeong, J. H. (1995). On the identification of a vortex. *Journal of Fluid Mechanics*, 285, 69-94.